

A Galerkin-Collocation domain decomposition method: application to the evolution of cylindrical gravitational waves

W. O. Barreto,^{1,2} J. A. Crespo,² H. P. de Oliveira,² and E. L. Rodrigues³

¹*Centro de Física Fundamental, Universidad de Los Andes, Mérida 5101, Venezuela*

²*Departamento de Física Teórica - Instituto de Física A. D. Tavares
Universidade do Estado do Rio de Janeiro*

R. São Francisco Xavier, 524. Rio de Janeiro, RJ, 20550-013, Brazil

³*Instituto de Biociências - Departamento de Física*

Universidade Federal do Estado do Rio de Janeiro

Av. Pasteur, 458 - Urca. Rio de Janeiro, RJ, 22290-040, Brazil

(Dated: February 2, 2018)

We present an innovative Galerkin-Collocation domain decomposition algorithm applied to the evolution of cylindrical unpolarized gravitational waves. We display how the domain decomposition effectiveness was successfully implemented for those initial data with localized high gradients. We have characterized the gravitational radiation using the standard Weyl scalar using the Newman-Penrose tetrad. Thus, it was possible to unveil aspects of the interaction between both gravitational polarization wave modes by generating the corresponding templates at the radiation zone.

I. INTRODUCTION

In the last years, we have witnessed the growing popularity of spectral methods in numerical relativity with applications in a large variety of problems [1]. The main advantage of spectral methods when compared with the traditional finite difference methods is the superior accuracy for a fixed number of grid points [2]. In particular, for smooth functions, the convergence rate exhibited by spectral methods is exponential. On the other hand, the accuracy of spectral methods in solving partial differential equations is drastically reduced in the case the solutions have localized regions of rapid variations, or if the spatial domain has a complex geometry [3, 4].

Multidomain techniques [3, 5–8] or simply the domain decomposition method is a beautiful and efficient strategy to improve the accuracy of spectral approximations for the cases mentioned above. The spatial domain is divided into two or more subdomains, where we can establish spectral approximations of a function in each subdomain together with the matching or transmissions conditions across the subdomains boundaries. In this approach, we have the set up of the spectral fixed mesh refinement.

In numerical relativity, the first applications of the domain decomposition technique involved the determination of the stationary configurations [9] and the initial data problem [10, 11], mainly for binaries of black holes. For the time-dependent systems, the spectral domain decomposition was implemented within the SpEC [12] and LORENE [13] codes to deal with the gravitational collapse, the dynamics of stars and the evolution of single [14] and binary black holes [15].

We point out that a crucial step for the implementation the domain decomposition technique is the

treatment of the transmission conditions in the cases of non-overlapping and overlapping subdomains. Let us consider, for instance, non-overlapping subdomains. For the time-independent situations such as the initial data problem described by elliptic equations, it is necessary to guarantee the smoothness of a function and its normal derivative on the surface the subdomains touch. On the other hand, hyperbolic problems require, in general, different interface conditions than elliptic ones known as the upwind, downwind and average scheme [3, 6, 16]. Mainly, these schemes comprise the way in which the weights of the contributions from the subdomains to update the equation at the common interface.

The aim of the present work is twofold. First, we present an innovative Galerkin-Collocation domain decomposition algorithm to evolve general cylindrical gravitational waves. We have divided the physical spatial domain into two subdomains and introduced the corresponding computational subdomains which are the loci of the collocation points. The communication between the physical and the computational subdomains is established by distinct mappings that cover the whole spatial domain. Second, we explore the consequences of the interaction between the gravitational wave polarization modes by generating the wave templates associated with the polarization modes at the radiation zone. Although cylindrical gravitational waves do not represent a real physical situation, they provide a useful theoretical laboratory to investigate the interaction of the polarization wave modes [17].

We have divided the paper as follows. In the second Section, we present the basic equations of the unpolarized cylindrical gravitational waves. In the third Section, the Galerkin-Collocation domain decomposition method is described in details together

with the numerical scheme to evolve the field equations. Section 4 presents the code validation through numerical tests comparing the single and domain decomposition algorithms. We have discussed the physical aspects in Section 5 by first establishing the version of the peeling theorem for cylindrical spacetimes. Consequently, we have the expression for the Weyl scalar Ψ_4 that determines the templates of the gravitational waves associated with each polarization mode at the wave zone. In this case, we have provided a useful to look into the interaction between both polarization modes. We close this work with some final remarks in Section 6.

II. BASIC EQUATIONS

We have considered the general cylindrical line element originally proposed by Kompaneets [18] and Jordan et al. [19] in null coordinates,

$$ds^2 = -e^{2(\gamma-\psi)}(du^2 + 2 du d\rho) + e^{2\psi}(dz + \omega d\phi)^2 + \rho^2 e^{-2\psi} d\phi^2, \quad (1)$$

where u is the retarded null coordinate that foliates the spacetime in hypersurfaces $u = \text{constant}$ and (ρ, z, ϕ) are the usual cylindrical coordinates. The metric functions ψ , ω , γ depend on u and ρ . As a well-known important aspect of cylindrical spacetimes [20], the functions ψ and ω represent the two dynamical degrees of freedom of the gravitational field, in which ψ accounts for the polarization mode $+$ while ω the polarization mode \times [20]. The function γ plays the role of the gravitational energy of the system; it is connected to the C-energy [20–22], more precisely $\gamma(\rho, u)$ gives the total energy per unit length enclosed within a cylinder of radius ρ at the time u .

Following Refs. [23, 24] it is convenient to introduce a new radial coordinate y by

$$\rho = y^2, \quad (2)$$

and to define the new fields $\bar{\psi}$ and $\bar{\omega}$, respectively by

$$\bar{\psi} = y\psi \quad (3)$$

$$\bar{\omega} = \frac{\omega}{y}. \quad (4)$$

The field equations in terms of the new fields $\bar{\psi}$ and $\bar{\omega}$ are expressed by

$$y\bar{\psi}_{,uy} - \frac{e^{\frac{4\bar{\psi}}{y}}}{2y}(\bar{y}\bar{\omega})_{,y}\bar{\omega}_{,u} - \frac{1}{4} \left[y \left(\frac{\bar{\psi}}{y} \right)_{,y} \right]_{,y} + \frac{e^{\frac{4\bar{\psi}}{y}}}{8y^3}(\bar{y}\bar{\omega})_{,y}^2 = 0 \quad (5)$$

$$y\bar{\omega}_{,uy} + \frac{2}{y}(\bar{y}\bar{\omega})_{,y}\bar{\psi}_{,u} + 2y \left(\frac{\bar{\psi}}{y} \right)_{,y} \bar{\omega}_{,u} - \frac{y^2}{4} \left[\frac{(\bar{y}\bar{\omega})_{,y}}{y^3} \right]_{,y} - \frac{1}{y}(\bar{y}\bar{\omega})_{,y} \left(\frac{\bar{\psi}}{y} \right)_{,y} = 0, \quad (6)$$

where the subscripts u and y denote partial derivatives with respect to these coordinates.

The dynamics of cylindrical spacetimes is fully described by the coupled wave equations (5) and (6) for the gravitational potentials $\bar{\psi}, \bar{\omega}$ starting with the initial data functions $\bar{\psi}_0(y) = \bar{\psi}(u_0, y)$ and $\bar{\omega}_0(y) = \bar{\omega}(u_0, y)$. These initial distributions are free of any constraint according with the characteristic scheme we adopt here.

The metric function γ satisfies the remaining field equations

$$\gamma_{,y} = \frac{y}{2} \left(\frac{\bar{\psi}}{y} \right)_{,y}^2 + \frac{e^{\frac{4\bar{\psi}}{y}}}{8y^3}(\bar{y}\bar{\omega})_{,y}^2 \quad (7)$$

$$\gamma_{,u} = \bar{\psi}_{,u} \left(\frac{\bar{\psi}}{y} \right)_{,y} - 2\bar{\psi}_{,u}^2 + \frac{e^{\frac{4\bar{\psi}}{y}}}{4y^2}[\bar{\omega}_{,u}(\bar{y}\bar{\omega})_{,y} - 2y^2\bar{\omega}_{,u}^2]. \quad (8)$$

Thus, the evolution of $\gamma(u, y)$ is determined after solving the wave equations (5) and (6).

The boundary conditions embody the well behaved coordinates as well as the regularity for the spacetime. After a careful inspection of the field equations (5) and (6), the conditions of regularity and flatness of the metric near the origin $y = 0$ impose that

$$\bar{\psi}(u, y) = \mathcal{O}(y) \quad (9)$$

$$\bar{\omega}(u, y) = \mathcal{O}(y^3). \quad (10)$$

The second boundary conditions are specified at the outer boundary or at the future null infinity, \mathcal{I}^+ ($y = \infty$). It can be shown [21] that the asymptotic analysis of the wave equations (5) and (6) results in

$$\bar{\psi}(u, y) = \bar{\psi}_\infty(u) + \mathcal{O}(y^{-1}), \quad (11)$$

$$\bar{\omega}(u, y) = \bar{\omega}_\infty(u) + \mathcal{O}(y^{-2}), \quad (12)$$

where $\bar{\psi}_\infty(u)$ and $\bar{\omega}_\infty(u)$ are arbitrary functions. Then, the spacetime is not asymptotically flat.

III. THE GALERKIN-COLLOCATION DOMAIN DECOMPOSITION METHOD

We present here the domain decomposition algorithm for the dynamics of general cylindrical gravitational waves. In Ref. [24] we have implemented a single domain method for the same problem. However, we have made a comment about the lack of exponential convergence using the single domain code to testing it against the Xanthopoulos exact solution [25] that contains both gravitational degrees of freedom $\bar{\psi}$ and $\bar{\omega}$. In general, the exact profiles exhibit rapid variations of the corresponding fields that spoil the exponential convergence for the case of one domain code. A domain decomposition algorithm improves the convergence as we indicated briefly in [24]. In what follows, we present the details.

We begin by dividing the spatial domain in two subdomains: $\mathcal{D}_1 : 0 \leq y \leq y_0$ and $\mathcal{D}_2 : y_0 \leq y < \infty$, where $y = y_0$ is the interface between both domains. The equivalent computational subdomains are indicated by $\mathcal{D}_A : -1 \leq x^{(A)} \leq 1$, with $A = 1, 2$ (cf. Fig. 1). We have chosen the following maps that connect the computational and physical subdomains:

$$\mathcal{D}_1 : y = \frac{y_0}{2}(1 + x^{(1)}), \quad (13)$$

$$\mathcal{D}_2 : y = y_0 + L_0 \frac{(1 + x^{(2)})}{(1 - x^{(2)})}, \quad (14)$$

where L_0 is the map parameter.

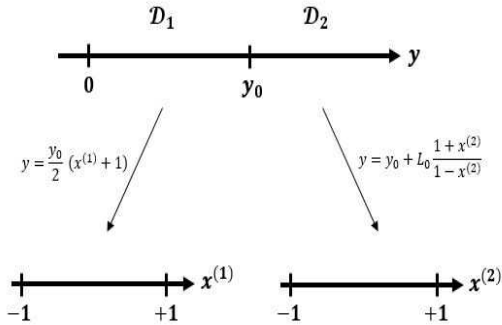


FIG. 1. Basic scheme showing the subdomains $\mathcal{D}_1 : 0 \leq y \leq y_0$ and $\mathcal{D}_2 : y_0 \leq y < \infty$ and the corresponding maps to the computational variable $x^{(A)}$ where $-1 \leq x^{(A)} \leq 1$ with $A = 1, 2$.

In each subdomain \mathcal{D}_A , $A = 1, 2$, we establish the spectral approximations for the gravitational potentials $\bar{\psi}$ and $\bar{\omega}$ as

$$\bar{\psi}^{(A)}(u, y) = \sum_{k=0}^{N_\psi^{(A)}} a_k^{(A)}(u) \Psi_k^{(A)}(y) \quad (15)$$

$$\bar{\omega}^{(A)}(u, y) = \sum_{k=0}^{N_\omega^{(A)}} b_k^{(A)}(u) \Phi_k^{(A)}(y), \quad (16)$$

where $N_\psi^{(A)}$ and $N_\omega^{(A)}$ are the truncations orders, not necessarily equal, that dictate the number of unknown modes $a_j^{(A)}(u)$ and $b_k^{(A)}(u)$, respectively. According to the Galerkin method, the basis functions $\Psi_j^{(A)}(y)$ and $\Phi_k^{(A)}(y)$ satisfy the boundary conditions (9) - (12) by combining conveniently the rational Chebyshev polynomials defined in each subdomain. The rational Chebyshev polynomials [26] defined in each subdomain are

$$TL_k^{(1)}(y) = T_k \left(x^{(1)} = \frac{2y}{y_0} - 1 \right), \quad (17)$$

$$TL_k^{(2)}(y) = T_k \left(x^{(2)} = \frac{y - y_0 - L_0}{y - y_0 + L_0} \right). \quad (18)$$

where $T_k(x)$ represents the standard Chebyshev polynomial of k th-order. We present below the basis functions:

$$\Psi_k^{(1)}(y) = \frac{1}{2}(TL_{k+1}^{(1)}(y) + TL_k^{(1)}(y)), \quad \Psi_k^{(2)}(y) = TL_k^{(2)}(y) \quad (19)$$

$$\Phi_k^{(2)}(y) = \Psi_k^{(2)}(y) = TL_k^{(2)}(y),$$

and the corresponding expression to $\Phi_k^{(1)}(y)$ can be found in the Appendix A.

We have followed the domain decomposition method straightforwardly for hyperbolic problems according to Gottlieb and Orszag [5]. In their approach, the junction or transmission conditions are

$$\begin{aligned} \bar{\psi}^{(1)}(u, y_0) = \bar{\psi}^{(2)}(u, y_0), \quad \left(\frac{\partial \bar{\psi}^{(1)}}{\partial y} \right)_{y_0} &= \left(\frac{\partial \bar{\psi}^{(2)}}{\partial y} \right)_{y_0} \\ \bar{\omega}^{(1)}(u, y_0) = \bar{\omega}^{(2)}(u, y_0), \quad \left(\frac{\partial \bar{\omega}^{(1)}}{\partial y} \right)_{y_0} &= \left(\frac{\partial \bar{\omega}^{(2)}}{\partial y} \right)_{y_0}. \end{aligned} \quad (20)$$

Taking into account the spectral approximations of the metric functions (15) and (16) into the above transmission conditions, we obtain four linear equations involving the coefficients $a_k^{(A)}(u)$ and $b_k^{(A)}(u)$,

$A = 1, 2$. Furthermore, these relations are used to reduce the total number of independent coefficients of $\bar{\psi}^{(A)}$ and $\bar{\omega}^{(A)}$ to $N_{\psi}^{(1)} + N_{\psi}^{(2)} + 2 - 2 = N_{\psi}^{(1)} + N_{\psi}^{(2)}$ and $N_{\omega}^{(1)} + N_{\omega}^{(2)} + 2 - 2 = N_{\omega}^{(1)} + N_{\omega}^{(2)}$, respectively.

$$\begin{aligned} \text{Res}_{\psi}^{(A)}(u, y) &= y\bar{\psi}_{,uy}^{(A)} - \frac{e^{\frac{4\bar{\psi}^{(A)}}{y}}}{2y}(y\bar{\omega}^{(A)})_{,y}\bar{\omega}_{,u}^{(A)} - \frac{1}{4}\left[y\left(\frac{\bar{\psi}^{(A)}}{y}\right)_{,y}\right] + \frac{e^{\frac{4\bar{\psi}^{(A)}}{y}}}{8y^3}(y\bar{\omega}^{(A)})^2_{,y} \\ \text{Res}_{\omega}^{(A)}(u, y) &= y\bar{\omega}_{,uy}^{(A)} + \frac{2}{y}(y\bar{\omega}^{(A)})_{,y}\bar{\psi}_{,u}^{(A)} + 2y\left(\frac{\bar{\psi}^{(A)}}{y}\right)_{,y}\bar{\omega}_{,u}^{(A)} - \frac{y^2}{4}\left[\frac{(y\bar{\omega}^{(A)})_{,y}}{y^3}\right]_{,y} - \frac{1}{y}(y\bar{\omega}^{(A)})_{,y}\left(\frac{\bar{\psi}^{(A)}}{y}\right)_{,y}. \end{aligned} \quad (21)$$

In general the residuals $\text{Res}_{\psi}^{(A)}(u, y)$ and $\text{Res}_{\omega}^{(A)}(u, y)$ do not vanish since $\bar{\psi}^{(A)}$ and $\bar{\omega}^{(A)}$ are approximations to the exact corresponding gravitational potentials. In according with the numerical strategy we are adopting, we use the Collocation method in the sense that the residual equations vanish at the collocation or grid points. Schematically we may write

$$\text{Res}_{\psi}^{(A)}(u, y_k) = 0, \quad k = 0, 1, \dots, N_{\psi}^{(A)} - 1 \quad (22)$$

$$\text{Res}_{\omega}^{(A)}(u, y_k) = 0, \quad k = 0, 1, \dots, N_{\omega}^{(A)} - 1, \quad (23)$$

where y_k denotes the collocation points in the physical subdomains. We have calculated these collocation points from the Chebyshev-Gauss points $x_k^{(A)}$

$$x_k^{(A)} = \cos\left(\frac{(2k+1)\pi}{2N^{(A)}}\right), \quad k = 0, 1, \dots, N^{(A)} - 1, \quad (24)$$

and the maps (13) and (14). Here $N^{(A)}$ denotes either $N_{\psi}^{(A)}$ or $N_{\omega}^{(A)}$.

We have approximated the field equations into a set of ordinary differential equations written in the following matricial form

$$\mathbf{M} \begin{pmatrix} \partial\bar{\psi}_k^{(1)} \\ \partial\bar{\psi}_k^{(2)} \\ \partial\bar{\omega}_j^{(1)} \\ \partial\bar{\omega}_j^{(2)} \end{pmatrix} = \mathbf{B} \quad (25)$$

for all $k = 0, 1, \dots, N_{\psi}^{(A)} - 1$ and $j = 0, 1, \dots, N_{\omega}^{(A)} - 1$. In the above expression we have

We proceed by establishing the residual equations by substituting the approximations (15) and (16) into the field equations (5) and (6) which yields

$$\partial\bar{\psi}_k^{(A)}(u) \equiv \left(\frac{\partial\bar{\psi}^{(A)}}{\partial u}\right)_k = \sum_{i=0}^{N_{\psi}} a_{i,u}^{(A)}(u)\Psi_i^{(A)}(y_k) \quad (26)$$

$$\partial\bar{\omega}_j^{(A)}(u) \equiv \left(\frac{\partial\bar{\omega}^{(A)}}{\partial u}\right)_j = \sum_{i=0}^{N_{\omega}} b_{i,u}^{(A)}(u)\Phi_i^{(A)}(y_k) \quad (27)$$

where $\partial\bar{\psi}_k^{(A)}(u)$ and $\partial\bar{\omega}_j^{(A)}(u)$ are the values of the derivatives of $\bar{\psi}^{(A)}$ and $\bar{\omega}^{(A)}$ with respect to u at the collocation points. Note that these values are related to the time derivatives of the unknown modes $a_{k,u}^{(A)}(u), b_{j,u}^{(A)}(u)$. The matrices \mathbf{M} and \mathbf{B} depend on the unknown modes $a_k^{(A)}(u), b_j^{(A)}(u)$ as well the values of $\bar{\psi}^{(A)}$ at the collocation points, or

$$\bar{\psi}_k^{(A)}(u) \equiv \bar{\psi}^{(A)}(u, y_k) = \sum_{i=0}^{N_{\psi}} a_i^{(A)}(u)\Psi_i^{(A)}(y_k), \quad (28)$$

that provides a set of relations between the values and the unknown modes. The integration is performed as follows: starting from the initial modes $a_k^{(A)}(u_0), b_k^{(A)}(u_0)$ we can determine the initial values $\bar{\psi}_k^{(A)}(u_0)$ as well the initial matrices \mathbf{M}, \mathbf{B} . The dynamical system gives the initial values $\partial\bar{\psi}_k^{(A)}(u_0), \partial\bar{\omega}_j^{(A)}(u_0)$ that allows to determine $a_{k,u}^{(A)}(u_0), b_{k,u}^{(A)}(u_0)$, and as a consequence, the modes at the next time step repeating the whole process. We have used a fourth-order Runge-Kutta integrator in all cases.

IV. NUMERICS

A very informative manner of presenting the advantage of the domain decomposition algorithm over

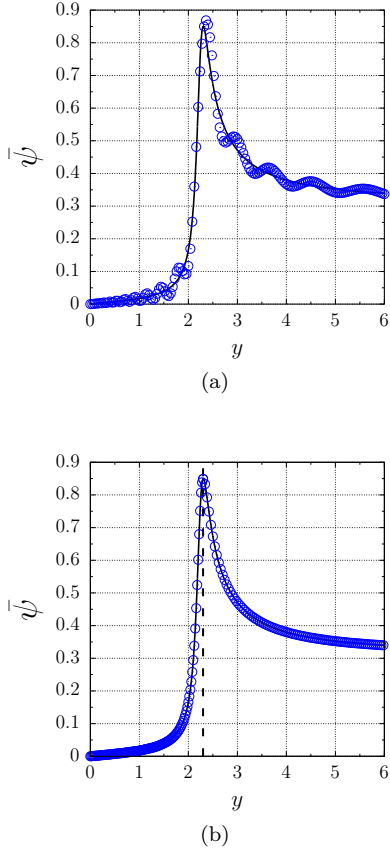


FIG. 2. Exact initial profile provided by the Weber-Wheeler solution (see Eq. B1) with $A_0 = 1.0$, $a = 2$ and $u_0 = -10$. In both graphs, the continuous lines and the circles correspond to the exact and the numerical solutions, respectively. It becomes clear that the numerical solution generated by the single domain algorithm with $N_\psi = 60$ (first panel) is less accurate than the one obtained with the domain decomposition algorithm with $N_\psi^{(1)} = N_\psi^{(2)} = 20$ (second panel). We have used $L_0 = 3$ in both cases, and the interface is placed at $y_0 = 2.3$.

the single domain algorithm we have developed in Ref. [24] is to reproduce some exact initial profiles of the gravitational potentials numerically. In the first example, we have considered the exact Weber-Wheeler [27] solution that corresponds to the case $\omega = 0$. The exact solution $\psi_{\text{exact}} = \psi_{\text{exact}}(u, y)$ shown in the Appendix B has two parameters, A_0 and a identified as the amplitude and the width of the wave, respectively. We have set $A_0 = 1$, $a = 2$ and $u_0 = -10$ to characterize the initial profile. The corresponding numerical profiles derived using the single domain algorithm [24] with $N_\psi = 60$ and the domain decomposition algorithm taking the truncation orders $N_\psi^{(1)} = N_\psi^{(2)} = 20$ are shown in Fig. 2. It

is evident the effectiveness of the domain decomposition in reproducing the initial profile with a smaller global truncation order. By increasing the truncation order for the single domain approximation we eventually arrive at a satisfactory numerical profile, but although not presented here the decay of the error between the exact and numerical profiles does not decay exponentially.

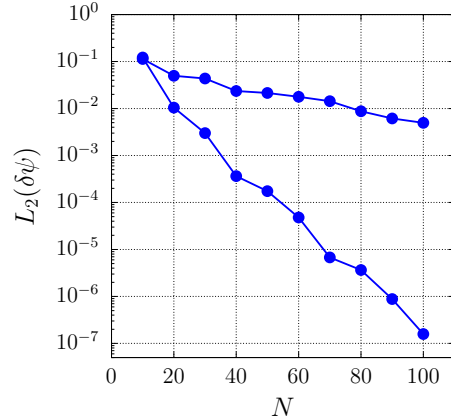


FIG. 3. The decay of the $L_2(\delta\psi)$ -error associated with the initial profile of Fig. 2, where $\delta\psi = \psi_{\text{exact}}(y) - \psi_{\text{numeric}}(y)$. We have evaluated the error in the computational domain as $L_2(\delta\psi) = \left[\frac{1}{2} \int_{-1}^1 (\delta\psi)^2 dx \right]^{\frac{1}{2}}$ and $L_2(\delta\psi) = \left[\frac{1}{2} \sum_{A=1}^2 \int_{-1}^1 (\delta\psi^{(A)})^2 dx \right]^{\frac{1}{2}}$ for the single and the domain decomposition algorithms, respectively. The horizontal axes stands for the truncation orders for the single domain, $N_\psi = N$, and for the domain decomposition where $N_\psi^{(1)} + N_\psi^{(2)} = N$ and $N_\psi^{(1)} = N_\psi^{(2)}$. The exponential decay of the error is much more accentuated for the domain decomposition algorithm as expected.

In the second example, we have borrowed the initial profiles of both gravitational potentials from the exact Xanthopoulos solution [25] (Appendix B). We have chosen $u_0 = -10$ and the same truncation orders as adopted before, i.e., for the single domain $N_\psi = N_\omega = 60$, and for the domain decomposition $N_\psi^{(A)} = 20$, $N_\omega^{(A)} = 20$, $A = 1, 2$. Fig. 3 displays the results of both potentials together with their respective numerical approximations.

In the third test, we have verified the global energy conservation using the Bondi formula (derived by Stachel [21]) in the present context. Briefly, the Bondi formula reads as

$$\frac{dM}{du} = - \left[\left(\frac{dc_1}{du} \right)^2 + \left(\frac{dc_2}{du} \right)^2 \right], \quad (29)$$

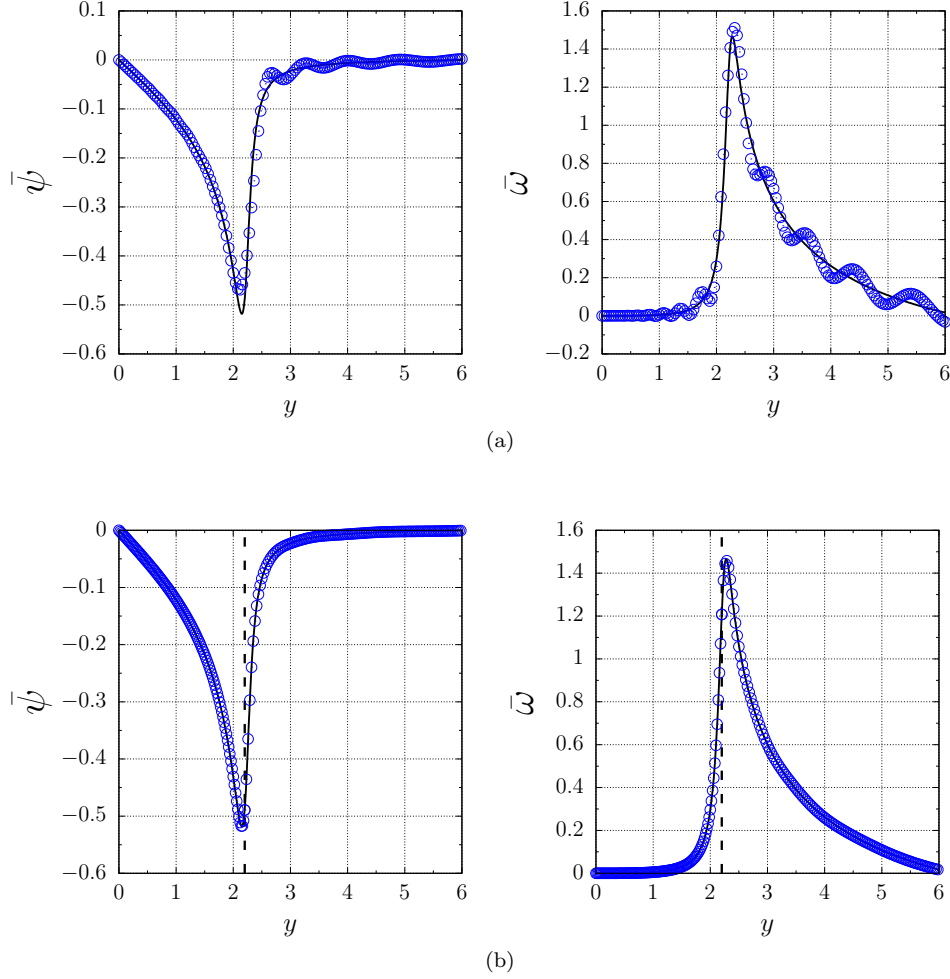


FIG. 4. Initial exact profile provided by the Xanthopoulos' solution. We have set $u_0 = -10$, $L_0 = 3$ and we have placed the interface at $y_0 = 2.3$. As before indicate the numerical solution and the continuous lines the exact solution. In (a) and (b) we have generated the results using the single and the domain decomposition algorithms, respectively.

where $M(u)$ is the Bondi mass aspect (indeed mass per unit of length), dc_1/du and dc_2/du are the news functions associated to each degree of freedom of the gravitational waves. We can calculate these quantities according to

$$M(u) = \frac{1}{2} \lim_{y \rightarrow \infty} \gamma \quad (30)$$

$$\frac{dc_1}{du} \equiv \lim_{y \rightarrow \infty} \bar{\psi}_{,u} \quad (31)$$

$$\frac{dc_2}{du} \equiv \lim_{y \rightarrow \infty} \left(\frac{e^{2\bar{\psi}/y\bar{\omega}}}{2} \right)_{,u} \quad (32)$$

To measure any deviation from the Bondi formula due to the numerical solution, we have written conveniently the Eq. (29) as

$$\mathcal{C}(u) = \left| 1 - \frac{M(u)}{M_0} - \frac{1}{M_0} \int_{u_0}^u \left[\left(\frac{dc_1}{du} \right)^2 + \left(\frac{dc_2}{du} \right)^2 \right] du \right| \times 100 \quad (33)$$

where $M_0 = M(u_0)$ is the initial Bondi mass. We have considered the initial data of Fig. 4 for which $u_0 = -10$ and $p = 0.9$. We have proceeded using equal truncation orders $N_\psi^{(A)} = N_\omega^{(A)} = N$ in both domains. Fig. 5 shows the exponential decay of the maximum value of $\mathcal{C}(u)$.

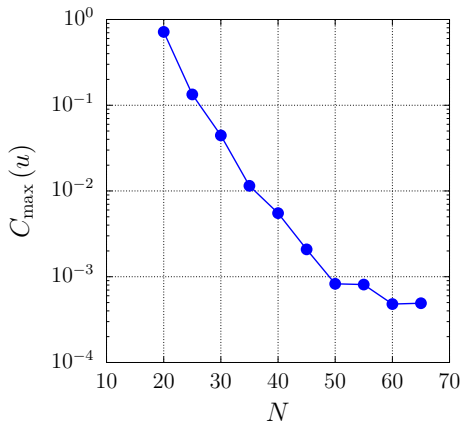


FIG. 5. Exponential decay of the maximum deviation of the energy conservation, C_{\max} (cf. Eq. (33)), for each truncation orders $N = N_{\psi}^{(A)} = N_{\omega}^{(A)} = N$, $A = 1, 2$, at each domain. The initial data is provided by the exact Xanthopoulos solution shown in Fig. 4. We have set the interface location and the map parameter as $y_0 = 2.3$, $L_0 = 3.0$, respectively. For $N > 60$ the maximum error approaches to its saturation value.

V. TEMPLATES OF THE GRAVITATIONAL WAVES

The peeling theorem plays a crucial role in characterizing the gravitational radiation emitted by an isolated source. After the works of Sachs [28] and Newman and Penrose [29], all the information containing in the Weyl tensor is expressed by five complex scalars known as the Weyl scalars. We denote these quantities by Ψ_n , $n = 0, 1, \dots, 4$, obtained after a convenient projection of the Weyl tensor in a null complex tetrad basis.

We can summarize the peeling theorem by the following behaviors of the Weyl scalars in a neighborhood of the future null infinity \mathcal{J}^+ :

$$\Psi_n \sim \frac{1}{r^{5-n}}, \quad (34)$$

where r is the affine parameter along the null rays. In particular, the Weyl scalar Ψ_4 falls off as r^{-1} indicating that the gravitational field behaves like a plane wave asymptotically. Therefore, if distinct from zero, Ψ_4 provides a measure of the outgoing gravitational wave at the radiation zone, or at a large distance from the source. As a consequence, we can express the Peeling theorem [28] in terms of the Weyl tensor projected with respect to the null tetrad basis such that

$$C_{abcd} = \frac{N_{abcd}}{r} + \frac{III_{abcd}}{r^2} + \frac{II_{abcd}}{r^3} + \frac{I_{abcd}}{r^4} + \dots, \quad (35)$$

where $N_{abcd}, III_{abcd}, \dots$ denote tensors with the algebraic structure of the Riemann tensors of Petrov types N, III, \dots , respectively. Those spacetimes of type N contain gravitational radiation whose templates associated to each polarization mode are given by the real and imaginary parts of N_{abcd} or

$$N_{abcd} \equiv (r\Psi_4)_{\infty} = \lim_{r \rightarrow \infty} r\Psi_4. \quad (36)$$

Stachel [21] has exhibited a version of the peeling theorem for the general cylindrical spacetimes, but the asymptotic expansion of the Riemann tensor is with inverse integer powers of $\rho^{\frac{1}{2}}$ since the spacetime is not asymptotically flat. It means that the Weyl scalars fall off as

$$\Psi_n \sim \frac{1}{y^{5-n}}. \quad (37)$$

Hence, for cylindrical spacetimes the Weyl scalar Ψ_4 describes the outgoing gravitational radiation at the wave zone. By choosing a convenient null tetrad basis shown in the Appendix C, the following real and imaginary parts provides the template of the waves at the wave zone corresponding to the mode $+$ and \times , respectively

$$\begin{aligned} (y\Psi_4)_{\infty} &= \lim_{y \rightarrow \infty} e^{-2\gamma} (2\bar{\psi}_{,u}\gamma_{,u} - \bar{\psi}_{,uu}) \\ &+ i \lim_{y \rightarrow \infty} \frac{1}{2} e^{-2\gamma} (-2\bar{\omega}_{,u}\gamma_{,u} + \bar{\omega}_{,uu}). \end{aligned} \quad (38)$$

It is worth remarking that the gravitational potentials are defined in the whole spatial domain so that in the above limits, we have used the approximations (15) and (16) with $A = 2$. The asymptotic expressions for $\gamma(u, y)$ and $\gamma_{,u}(u, y)$ are calculated from Eqs. (30) and (8), respectively, producing the final expressions in function of the modes $a_k^{(2)}, b_k^{(2)}$

We have considered the exact Weber-Wheeler wave that has only the real part of the Eq. (36) describing the outgoing wave template at the radiation zone. We have evolved the Weber-Wheeler wave numerically starting from the initial data shown in Fig. 2 with truncation orders $N_{\psi}^{(1)} = N_{\psi}^{(2)} = 40$. In Fig. 6 we present the agreement between the exact (line) and the numerical (circles) wave templates that serve as an additional illustration of the accuracy of the domain decomposition technique. It

is also noteworthy mentioning the simple structure of the polarized Weber-Wheeler wave after hitting the symmetry axis and rebounding back to infinity. Also, we have verified that the template does not change significantly with the parameter a .

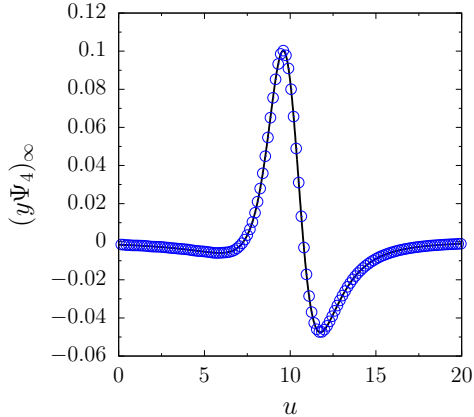


FIG. 6. The template of the exact Weber-Wheeler wave given by the behavior of $(y\Psi_4)_\infty$ (continuous line) together with the corresponding numerical solution. Again, the agreement of the numerical solution between both solutions illustrates the excellent accuracy of the domain decomposition code. We have set $N_\psi^{(1)} = N_\psi^{(2)} = 40$, $y_0 = 2.4$ and $L_0 = 2$. The initial configuration corresponding to the above signal is the same of Fig. 2.

The Einstein-Rosen waves [30] are the most general polarized gravitational waves. We have generated wave templates starting with distinct initial data families

$$\bar{\psi}_0(y) = A_0 y^n e^{-\frac{(y-y_1)^2}{\sigma^2}} \quad (39a)$$

$$\bar{\psi}_0(y) = A_0 y^2 \left[1 - \tanh \left(\frac{(y-y_2)^2}{\sigma^2} \right) \right], \quad (39b)$$

where we have fixed $\sigma = 0.5$, $y_1 = y_2 = 3.0$ and $n \geq 1$. We have observed that for the Gaussian profile the wave template is not altered substantially for $n = 1, 2, 3, 4$, but for the second initial profile (39b), the template exhibits a small but noticeable change as shown in Fig. 7.

The last wave templates we are going to exhibit correspond to the unpolarized cylindrical gravitational waves. The initial profiles for both potentials

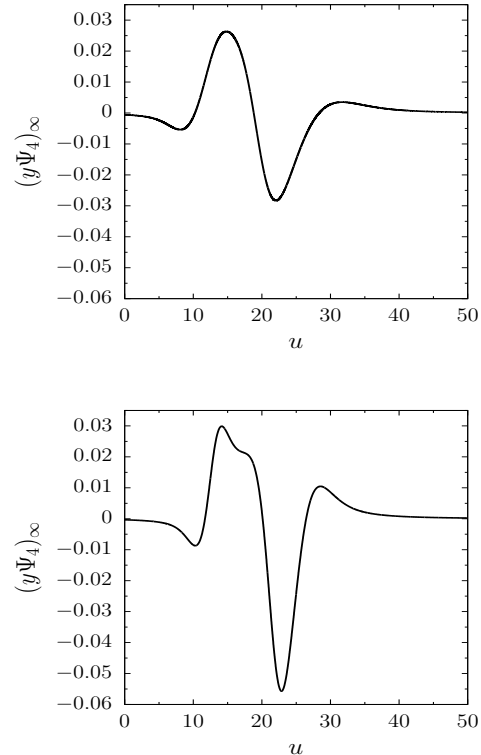


FIG. 7. The wave templates for the Einstein-Rosen waves generated by the initial data families (36) and (37) shown by the upper and lower panels, respectively. We have set $y_1 = y_2 = 30$, $n = 1$ and $\sigma = 0.5$.

are

$$\bar{\psi}_0(y) = A_0 y^2 e^{-(y-y_1)^2/\sigma_1^2} \quad (40a)$$

$$\bar{\omega}_0(y) = \frac{B_0 y^3}{1+y^2} e^{-(y-y_2)^2/\sigma_2^2}, \quad (40b)$$

where the parameters A_0 and B_0 play the roles of the initial amplitudes of the wave modes, the constants y_1, y_2 and σ_1, σ_2 denote the position and widths of the waves, respectively. For the sake of convenience we have fixed $y_1 = y_2 = 3.0$ and $\sigma_1 = \sigma_2 = 0.5$.

The numerical experiments have consisted in evolving gravitational waves generated with fixed $A_0 = 0$ and varying the initial amplitude B_0 . It means that we start with a polarized gravitational wave mode \times , but due to the nonlinear interaction between both wave modes, a component $+$ wave is generated. Fig. 8 illustrates the effect of increasing B_0 in the wave templates described by the real (mode $+$) and the imaginary (mode \times) parts of Eq. (38). At first glance, it is noteworthy the relative

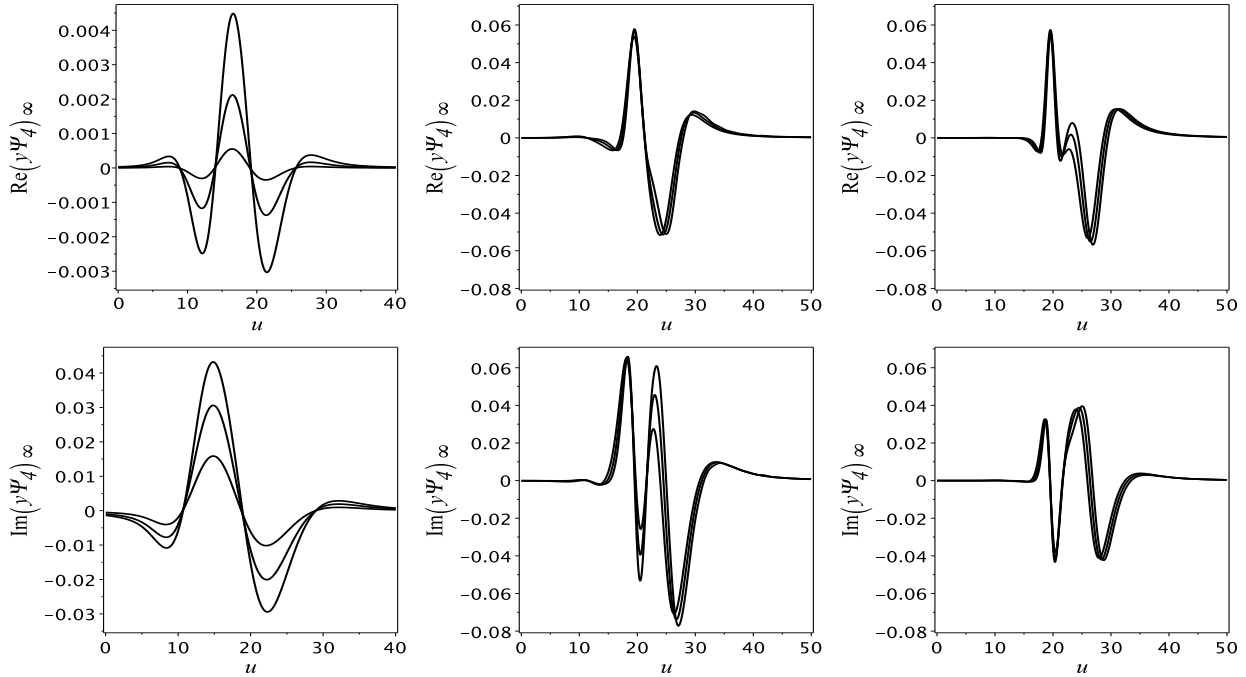


FIG. 8. Gravitational wave templates of the modes $+$ and \times shown by the upper and the lower panels, respectively. We have considered the initial data (40) with A_0 and $B_0 = 0.1, 0.2, 0.3$ in the column on the left, $B_0 = 1.6, 1.7, 1.8$ in the middle, and $B_0 = 2.0, 2.1, 2.2$ in the column on the right. Notice that the curves on the left column the maximum amplitude of $\text{Re}(y\Psi_4)_\infty$ has increased by an approximate factor 10 whereas the corresponding growth observed for $\text{Im}(y\Psi_4)_\infty$ was about 3. On the middle column the wave modes $+$ and \times exhibit amplitudes of the approximately same order of magnitude as the result of the interaction between the modes $+$ and \times . The panels on the right show a decrease of the wave signal amplitude of the mode \times as a consequence of the energy transfer to the mode $+$.

accentuated increase of the amplitude of $\text{Re}(y\Psi_4)_\infty$ from about 5.5×10^{-4} to 4.5×10^{-3} corresponding to $B_0 = 0.1$ and $B_0 = 0.3$, respectively. The imaginary part has increased its amplitude in a small amount, i.e., from about 0.015 to 0.045.

By increasing further B_0 , we have noticed that the maximum amplitude of the templates achieves the same order of magnitude. Fig. 9 shows the templates associated with each polarization mode for $B_0 = 1.6, 1.7$ and 1.8 . Also, the maximum amplitudes of each mode do not increase substantially, but the wave-forms are altered. As a final comment, the maximum amplitude of the wave mode $+$ has increased about 100 times when B_0 increased from 0.1 to 1.8, whereas the corresponding maximum amplitude of the wave mode \times increased approximately by a factor 6.

The accentuated growth of the wave mode $+$ as a consequence of the nonlinear interaction with the wave mode \times implies in more mass-energy extracted by the wave mode $+$. The quantities

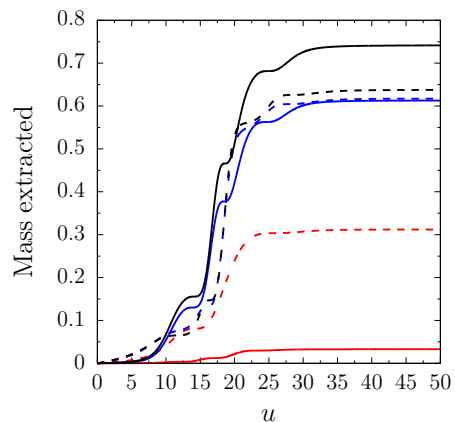


FIG. 9. Graphs of $I_+(u)$ (continuous lines) and $I_\times(u)$ (dotted lines) for $B_0 = 0.9, 1.7$ and 1.8 represented by the pair of red, blue and black curves, respectively.

$$I_+(u) = \int_{u_0}^u \left(\frac{dc_1}{du} \right)^2 du \quad (41)$$

$$I_\times(u) = \int_{u_0}^u \left(\frac{dc_2}{du} \right)^2 du \quad (42)$$

are the measures of the mass extracted by each wave mode. In Ref. [24] we have discussed rapid growth of $I_+(u)$ after fixing $A_0 = 0$ and increasing B_0 . At certain value $I_+(u)$ surpass $I_\times(u)$. We have called this property as the enhancement effect. In the present situation, we have found that $I_+(u) \approx I_\times(u)$ for $B_0 = 1.7$. We have exhibited the quantities $I_+(u)$ and $I_\times(u)$ for some values of B_0 , and it becomes clear that if $B_0 > 1.7$ the enhancement effect takes place.

VI. FINAL REMARKS

We have developed a version of the Galerkin-Collocation method with the technique of domain decomposition to evolve general cylindrical gravitational waves. The advantage of the domain decomposition over the single domain code becomes evident when the potentials $\psi(u, y)$ and $\bar{\omega}(u, y)$ have high gradients in some regions of the spatial domain.

We would like to highlight two relevant aspects. The first is the way we have introduced the computational domains schematically illustrated in Fig. 1 and described more precisely by the maps (13) and (14) that cover the whole spatial domain. The second aspect is, in general, the basis functions have a simple form if compared with those used in the single domain code (cf. Ref. [24]).

Most of the numerical tests consisted in comparing the numerical solutions generated in the single and double domains algorithms. Even for the initial profile given by the Weber-Wheeler solution corresponding to $u = -10$ the domain decomposition approximation showed to be far superior using a smaller number of collocation points. We also considered the Xanthopoulos solution to generate more general initial profiles for both gravitational potentials and again the numerical solution with domain decomposition showed to be better. The final test was the evolution of the Xanthopoulos solution with the verification of the global energy conservation.

As mentioned cylindrical gravitational waves do not reproduce a plausible astrophysical event, but might be relevant as an approximation near a long string or even another topological defect. Nonetheless, the quest for interacting gravitational wave modes $+$ and \times meets a valid theoretical laboratory in cylindrical symmetry. In this context, we

have taken advantage of the equivalent of the Peeling theorem to determine the templates of the polarized and unpolarized gravitational waves at the radiation zone. In the numerical experiments, we have excited initially only the \times wave mode ($A_0 = 0, B_0 \neq 0$, cf. Eqs. (40a) and (40b)) and due to the mutual nonlinear interaction between the wave modes, the component $+$ emerges. As the initial amplitude of the \times grows, a more accentuated growth of the amplitude of the mode $+$ until both wave modes have the corresponding template amplitudes of the same order of magnitude. Notice also that the waveforms at the radiation zone change with the increase of B_0 .

Finally, the relatively rapid growth of the wave mode $+$ reflects the enhancement effect characterized when this mode becomes dominant in extracting mass. It figures as a consequence of the nonlinear interaction between the wave modes. We believe that the investigation of this nonlinear interaction in a more realistic scenario such provided by the Bondi-Sachs problem is worthy of investigation.

ACKNOWLEDGMENTS

The authors acknowledge the financial support of the Brazilian agencies Conselho Nacional de Desenvolvimento Científico e Tecnológico (CNPq) and Coordenação de Aperfeiçoamento de Pessoal de Nível Superior (CAPES). H. P. O. thanks Fundação Carlos Chagas Filho de Amparo à Pesquisa do Estado do Rio de Janeiro (FAPERJ) for support within the Grant No. E-26/202.998/518 2016 Bolsas de Banca de Projetos (BBP).

Appendix A: Basis functions

First we define the auxiliary basis $\chi_k(y)$ as

$$\chi_k(y) = \frac{1}{2}TL_{k+2}^{(1)}(y) + \frac{k+1}{2k+1}TL_{k+1}^{(1)}(y) + \frac{2k+3}{4(2k+1)}TL_k^{(1)}(y) \quad (A1)$$

and the basis functions $\Phi_k^{(1)}(y)$ are

$$\Phi_k^{(1)}(y) = \frac{1}{4}\chi_k(y) + \frac{(2k^2+5k+3)}{4(2k^2+9k+9)}\chi_{k+1}(y). \quad (A2)$$

Appendix B: Exact solutions: the Weber-Wheeler and the Xanthopoulos solutions

The particular Weber-Wheeler solution is given by [27]

$$\psi_{\text{exact}}(u, y) = A_0 \sqrt{\frac{\sqrt{a^2 + y^4 + (u + y^2)^2 [2a^2 - 2y^4 + (u + y^2)^2]} + a^2 - u^2 - 2uy^2}{a^2 + y^4 + (u + y^2)^2 [2a^2 - 2y^4 + (u + y^2)^2]}}, \quad (\text{B1})$$

where A_0 and a are parameters identified as the amplitude and the width of the wave, respectively.

From Ref. [25] and after a straightforward calculation, the exact expressions for the potentials $\bar{\psi}$ and $\bar{\omega}$ in null coordinates $u, \rho = y^2$ are

$$\bar{\psi}_{\text{exact}}(u, y) = \frac{y}{2} \log \left[\frac{p^2(\eta^2 + \mu^2) + \mu^2 + 1}{(1 - p\eta)^2 + (1 + p^2)\mu^2} \right] \quad (\text{B2})$$

$$\bar{\omega}_{\text{exact}}(u, y) = \frac{2\sqrt{1 + p^2(\mu^2 - 1)(1 - p\eta)}}{py [p^2(\eta^2 + \mu^2) + \mu^2 - 1]} \quad (\text{B3})$$

where p is a free parameter, μ and η are functions of (u, y)

$$\mu(u, y) = \frac{\Delta}{\sqrt{2}} \quad (\text{B4})$$

$$\eta(u, y) = \frac{\sqrt{2}(u + y^2)}{\Delta}, \quad (\text{B5})$$

and

$$\Delta = \left[-u^2 - 2uy^2 + 1 + \sqrt{(-u^2 - 2uy^2 + 1)^2 + 4(u + y^2)^2} \right]^{1/2}. \quad (\text{B6})$$

The second parameter, α , appears in the expression of $\gamma(u, y)$ as

$$e^{2\gamma} = \frac{\alpha^2 [p^2(\eta^2 + \mu^2) + \mu^2 - 1]}{\eta^2 + \mu^2}. \quad (\text{B7})$$

Appendix C: The null tetrad basis

We can express components of the metric tensor with respect to a set of null tetrads as

$g_{\mu\nu} = -l_\mu k_\nu - k_\mu l_\nu + m_\mu \bar{m}_\nu + \bar{m}_\mu m_\nu$, (C1) where l_μ, k_μ and m_μ are null vectors that satisfy the relations $l_\mu k^\mu = -m_\mu \bar{m}^\mu = -1$. After a straightforward calculation we have

$$l_\mu = e^{2(\gamma - \psi)} \delta_\mu^0 \quad (\text{C2})$$

$$k_\mu = \frac{1}{2} \delta_\mu^0 + \delta_\mu^1 = \left(\frac{1}{2}, 1, 0, 0 \right) \quad (\text{C3})$$

$$m_\mu = \frac{1}{\sqrt{2}} (0, 0, e^\psi, \omega e^\psi - i\rho e^{-\psi}) \quad (\text{C4})$$

$$\bar{m}_\mu = \frac{1}{\sqrt{2}} (0, 0, e^\psi, \omega e^\psi + i\rho e^{-\psi}). \quad (\text{C5})$$

The Newman-Penrose scalar Ψ_4 is given by

$$\Psi_4 = R_{\mu\nu\alpha\beta} \bar{m}^\mu k^\nu \bar{m}^\alpha k^\beta, \quad (\text{C6})$$

and the corresponding real and imaginary parts are respectively

$$\begin{aligned} (\Psi_4)^{\text{real}} = & e^{2(\psi - \gamma)} \left[\frac{1}{2y} \left(\frac{\bar{\psi}, u}{y} \right)_{,y} - \frac{\bar{\psi}, uu}{y} - \frac{1}{16y^2} \left(\frac{\bar{\psi}}{y} \right)_{,yy} \right. \\ & + \frac{1}{16y^3} \left(\frac{\bar{\psi}}{y} \right)_{,y} + \left(\frac{1}{2y} \left(\frac{\bar{\psi}}{y} \right)_{,y} - 2 \frac{\bar{\psi}, u}{y} - \frac{1}{2y^2} \right) \times \\ & \left. \left(\frac{1}{4y} \gamma_{,y} - \gamma_{,u} \right) - \frac{1}{2} \left(\frac{1}{2y} \left(\frac{\bar{\psi}}{y} \right)_{,y} - 2 \frac{\bar{\psi}, u}{y} \right)^2 \right. \\ & \left. + \frac{e^{4\psi}}{2y^4} \left(\frac{1}{4y} (y\bar{\omega})_{,y} - y\bar{\omega}, u \right) \right] \quad (\text{C7}) \end{aligned}$$

$$\begin{aligned} (\Psi_4)^{\text{im}} = & \frac{1}{2y} e^{2(\psi - \gamma)} \left[\left(\frac{1}{2y^2} (y\bar{\omega})_{,y} - \bar{\omega}, u \right) \left(\frac{3}{2y} \left(\frac{\bar{\psi}}{y} \right)_{,y} - \frac{6\bar{\psi}, u}{y} \right. \right. \\ & \left. \left. - \frac{\gamma_{,y}}{2y} + 2\gamma_{,u} - \frac{1}{2y^2} \right) - \frac{(y\bar{\omega}, u)_{,y}}{2y^2} + \bar{\omega}, uu + \frac{1}{16y^3} \times \right. \\ & \left. \left((y\bar{\omega})_{,yy} - \frac{(y\bar{\omega})_{,y}}{y} \right) \right] \quad (\text{C8}) \end{aligned}$$

-
- [1] P. Grandclément and J. Novak, *Living Rev. Relativ.* (2009) 12: 1.
- [2] L. E. Kidder and L. S. Finn, *Phys. Rev. D* 62, 084026 (2000).
- [3] Claudio Canuto, Alfio Quarteroni, M. Yousuff Hus-saini and Thomas A. Zang, *Spectral Methods in Fluid Dynamics*, Springer-Verlag (1988).
- [4] D. Gottlieb and J. S. Hesthaven, *J. Comp. App. Math.* - Special issue on Numerical Analysis, vol VII: Partial Differential Equations, 128, 1-2, 83 (2001).
- [5] D. Gottlieb and S. A. Orszag, *Numerical Analysis of Spectral Methods: Theory and Applications*, SIAM (1977).
- [6] D. A. Kopriva, *App. Num. Math.* 2, 221 (1986).
- [7] S. Orszag, *J. Comp. Phys.* 37, 70 (1980).
- [8] D. A. Kopriva, *SIAM J. Sci. Stat. Comput.*, 10, 120 (1989).
- [9] S. Bonazzola, E.ourgoulhon, M. Salgado and J.-A. Marck, *Astron. Astrophys.*, 278, 421 (1993).
- [10] H. P. Pfeiffer, *Initial data for black hole evolutions*, Ph.D. thesis, arXiv:gr-qc/0510016 (2003).
- [11] M. Ansorg, *Class. Quantum Grav.*, 24 S1 (2007).
- [12] Spectral Einstein Code, <https://www.black-holes.org/code/SpEC.html>
- [13] LORENE (Langage Objet pour la RElativité Numérique), <http://www.lorene.obspm.fr>
- [14] L. E. Kidder, M. A. Scheel, and S. A. Teukolsky, *Phys. Rev. D* 62, 084032 (2000).
- [15] B. Szilágyi, L. Lindblom, and M. A. Scheel, *Phys. Rev. D* 80, 124010 (2009).
- [16] A. T. Patera, *J. Comp. Phys.* 54, 468 (1984).
- [17] T. Piran, P. N. Safer and R. F. Stark, *Phys. Rev. D* 32, 3101 (1985).
- [18] A. S. Kompaneets, *Zh. Eksp. Teor. Fiz.* 34, 953 (*Sov. Phys. JETP* 7 659, (1958)) (1958).
- [19] P. Jordan, J. Ehlers, and W. Kundt, *Abh. Akad. Wiss. Mainz. Math. Naturwiss. Kl* 2 (1960).
- [20] K. S. Thorne, *Phys. Rev.* 138, 251 (1965).
- [21] J. J. Stachel, *J. Math. Phys.*, 7, 1321 (1966).
- [22] S. M. C. V. Gonçalves, *Class. Quantum Grav.* 20, 37 (2003).
- [23] M. R. Dubal, R. A. d’Inverno and C. J. S. Clarke, *Phys. Rev. D* 52, 6868 (1995).
- [24] J. Celestino, H. P. de Oliveira and E. L. Rodrigues, *Phys. Rev. D* 93, 104018 (2016).
- [25] B. C. Xanthopoulos, *Phys. Rev. D* 34, 3608 (1986).
- [26] John Boyd, *Chebyshev and Fourier Spectral Methods*, Dover Publications (2001).
- [27] J. Weber and J. A. Wheeler, *Rev. Mod. Phys.* 29, 509 (1957).
- [28] R. K. Sachs, *Proc. Roy. Soc. A* 265, 463 (1962); *ibid.* A270, 103 (1962).
- [29] E. T. Newman and R. Penrose, *J. Math. Phys.* 3, 566 (1962); *J. Math. Phys.*, 4, 998 (1963).
- [30] A. Einstein and N. Rosen, *J. Franklin Inst.* 223, 43 (1937).